






Exploring quasifission dynamics in reactions leading to the formation of  $^{225}\text{Pa}$ 

K. Atreya <sup>1,2</sup> A. Sen,<sup>1,2</sup> T. K. Ghosh <sup>1,2,\*</sup> A. K. Nasirov <sup>3,4</sup> D. Paul,<sup>1,2</sup> Md. Moin Shaikh,<sup>1,†</sup> K. Banerjee,<sup>1,2</sup> C. Bhattacharya,<sup>1,2</sup> Samir Kundu,<sup>1,2</sup> S. Manna,<sup>1,2</sup> G. Mukherjee <sup>1,2</sup> S. Nandi,<sup>1,‡</sup> R. Pandey,<sup>1,2</sup> T. K. Rana,<sup>1,2</sup> Pratap Roy <sup>1,2</sup> S. Mukhopadhyay,<sup>1,2</sup> and Raj Kumar Santra<sup>1</sup>

<sup>1</sup>Variable Energy Cyclotron Centre, 1/AF, Bidhan Nagar, Kolkata 700064, India

<sup>2</sup>Homi Bhabha National Institute, Training School Complex, Anushakti Nagar, Mumbai - 400094, India

<sup>3</sup>Bogoliubov Laboratory of Theoretical Physics, JINR, 141980 Dubna, Russia

<sup>4</sup>Department of Physics, Institute of Nuclear Physics, Tashkent - 100174, Uzbekistan



(Received 7 March 2023; revised 2 May 2023; accepted 22 August 2023; published 21 September 2023)

**Background:** Understanding the dynamics of quasifission reactions for the pre-actinides and actinides is particularly important for choosing suitable target projectile combinations to synthesize of superheavy elements. Measurements of fission-fragment mass distributions by us in reactions populating the pre-actinides nuclei  $^{200}\text{Pb}$  showed no indication of the presence of quasifission, contrary to two recent claims from the state-of-the-art theoretical calculations that predicted noncompound nuclear reaction in these reactions.

**Purpose:** The purpose was to investigate the signature of noncompound nuclear fission, if any, in the fission of  $^{225}\text{Pa}$  populated via two different entrance channels  $^{20}\text{Ne} + ^{205}\text{Tl}$  and  $^{16}\text{O} + ^{209}\text{Bi}$ .

**Methods:** Two position-sensitive multiwire proportional counters were placed at the folding angle to detect the fission fragments. Mass distributions were extracted from the measured time-of-flight differences and position information ( $\theta$ ,  $\phi$ ) of the fission fragments.

**Results:** The mass distributions for both reactions are found to be symmetric at all the measured energies up to the excitation energy of 110 MeV. The variation of the standard deviations of mass distributions increases smoothly with excitation energy. The theoretical calculation indicates a significant amount of quasifission in the mass asymmetric region in both reactions.

**Conclusion:** The measured fission-fragment mass distributions for the two reactions that populated the same compound nucleus, do not provide evidence of quasifission in the mass symmetric region.

DOI: [10.1103/PhysRevC.108.034615](https://doi.org/10.1103/PhysRevC.108.034615)

## I. INTRODUCTION

Quasifission (QF) and fusion fission (FF) are two competing processes affecting the formation probability of superheavy elements (SHEs). To optimize the exploration of the SHE landscape, the key challenge is to understand the competition between QF and FF. Several experiments are being carried out worldwide [1,2] to understand the dynamics of QF and FF, although there is a scarcity of reliable dynamical models [3–6] that efficiently predict the amount of QF in a reaction. However, the new models that are being developed need to be validated experimentally.

In the reactions with heavy-ion beams around the Coulomb barrier energies, noncompound nuclear fission, such as fast-fission, QF, and pre-equilibrium fission [7–10] competes with fully equilibrated compound nuclear fission, called fusion fission. The fusion dynamics is strongly influenced by several entrance channel properties such as charge ( $Z$ ) product of target ( $t$ ) and projectile ( $p$ ) nuclei ( $Z_p Z_t$ ), charge and

mass asymmetry ( $Z$  and  $A$ ), shell effect, and collision energy [3,4,11]. Experimental investigation of mass-energy and angular distribution of fission products are employed for efficiently identifying compound and noncompound nuclear processes [12].

According to the standard statistical model of fission, the mass distribution of fission products follows Liquid Drop Model (LDM) predictions of symmetric mass distribution and the width of mass distribution varies smoothly as a function of excitation energy. A recent state-of-the-art theoretical calculation [13], performed in the framework of the di-nuclear system and advanced statistical models, predicted a dramatic increase in QF with an increase in excitation energies for the fusion of  $^{16}\text{O}$ ,  $^{19}\text{F}$  induced reactions on pre-actinide targets  $^{181}\text{Ta}$ ,  $^{184}\text{W}$ . This is surprising as  $Z_p Z_t$  for the entrance channel ( $<700$ ) is well below the expected charge product ( $\approx 1600$ ) to set in QF. Interestingly, measurement of fission-fragment mass distributions for these systems carried out by us [14] near the barrier energies indicated the absence of quasifission. It is, however, to be mentioned that the measurement [14] were restricted to near-barrier energies.

To further investigate the role of the entrance channel on fission-fragment mass distribution, we have measured the fission-fragment mass distribution for the  $^{20}\text{Ne} + ^{205}\text{Tl}$  ( $Z_p Z_t = 810$ ) and  $^{16}\text{O} + ^{209}\text{Bi}$  ( $Z_p Z_t = 664$ ) reactions, this

\*tilak@vecc.gov.in

<sup>†</sup>Present address: Chanchal College, Malda, West Bengal 732123, India.

<sup>‡</sup>Present address: Argonne National Laboratory, Argonne, Illinois 60439, USA.

time even at much higher energies beyond the Coulomb barrier, populating the same compound nucleus  $^{225}\text{Pa}$ . No significant deviation was observed between the two entrance channels and the monotonic increase in the variation of the width of the mass distributions with excitation energy indicates the absence of QF in the mass-symmetric region in either of the reactions. This is consistent with our earlier findings [14], which however, is contrary to the expectation of theoretical model calculations [13,15]. The measured mass distributions have been compared with the predictions from the model calculations [13]. The calculated mass distributions show a significant amount of QF events, however, only near the projectile or target mass region, far from the mass-symmetric events.

## II. EXPERIMENTAL DETAILS

The experiment was carried out at the Variable Energy Cyclotron Centre (VECC) in Kolkata, India. A  $^{20}\text{Ne}$  beam with energies ranging from 145 to 180 MeV and an  $^{16}\text{O}$  beam from 116 to 160 MeV were bombarded on  $^{205}\text{Tl}$  (with a thickness of  $300\ \mu\text{g}/\text{cm}^2$ ) and  $^{209}\text{Bi}$  ( $400\ \mu\text{g}/\text{cm}^2$ ) targets, respectively. The angle of the targets with respect to the axis of the beam was  $45^\circ$ . To detect fission fragments, two position-sensitive multiwire proportional counters (MWPCs) were mounted inside a general purpose scattering chamber on the two movable arms on both sides of the beam axis. These arms were positioned such that the detectors were placed at the calculated folding angle following the complete transfer of momentum from the projectile to the target. Viola's systematic [16] was used to calculate the folding angle for the symmetric fission events. Isobutane gas was maintained within the MWPCs at a constant pressure of 3.0 Torr. The time-of-flight of the fission fragments with respect to the cyclotron beam pulses, the  $X$  and  $Y$  coordinates, and the energy loss in each of the MWPCs were recorded. While one detector was placed at a fixed angle ( $90^\circ$ ), the other detector was maintained at an angle corresponding to the folding angle following Viola's systematic for symmetric fragmentation following fission. The  $X$  and  $Y$  coordinates of the MWPCs were calibrated using a  $^{252}\text{Cf}$  source and using this calibration, the emission angle for each of the fragments was calculated. Counts taken from the Faraday cup were used for beam flux monitoring and data normalization.

## III. DATA ANALYSIS AND RESULTS

The fission fragments were separated from elastic and quasi-elastic particles using the measured time and energy-loss correlation spectra in the analysis. The masses of the fission fragments were determined from the measured time-of-flight difference, azimuthal and polar angles, momentum, and recoil velocities for each event. The data analysis procedure was described in detail in our earlier reports [17–19]. It is to be mentioned that the method of calculation of masses of the fission fragments from the time-of-flight differences removes the uncertainty due to the time (radiofrequency) structure of the cyclotron beam.

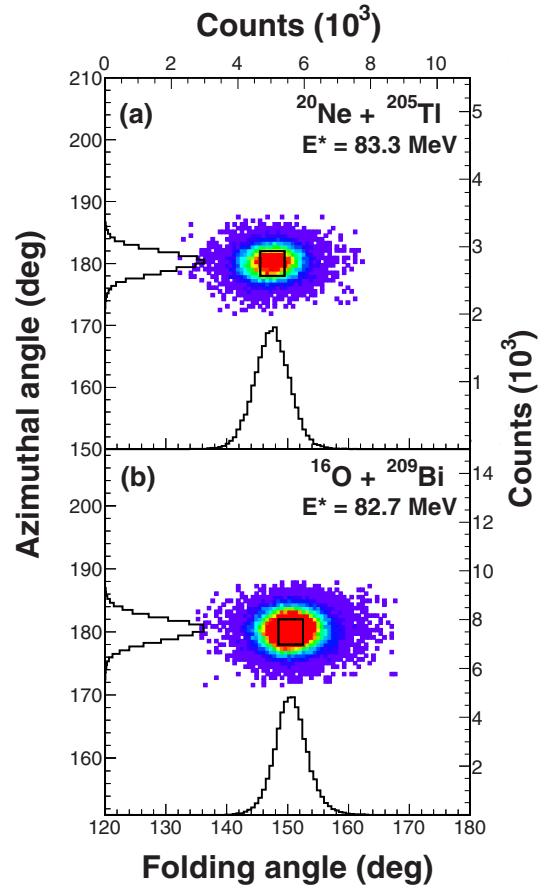


FIG. 1. Folding angle distributions of the complementary fission fragments for the reactions  $^{20}\text{Ne} + ^{205}\text{Tl}$  and  $^{16}\text{O} + ^{209}\text{Bi}$  at an excitation energy of  $\approx 83$  MeV. A gate (marked by the solid line) at the center of the distribution was used to separate fusion-fission events to determine mass distribution. The projections of the folding and azimuthal angles are also shown. The right and top axes indicate the counts corresponding to the projections of the folding angles and azimuthal angles, respectively.

Figure 1 shows the representative polar ( $\theta$ ) and azimuthal ( $\phi$ ) angular correlations for all the measured events in the  $^{20}\text{Ne} + ^{205}\text{Tl}$  and  $^{16}\text{O} + ^{209}\text{Bi}$  reactions at an excitation energy of  $\approx 83$  MeV. While the projections of azimuthal angle peaks at  $180^\circ$ , the projections of polar angle showed a single Gaussian folding angle distribution with the peak position which is consistent with the corresponding full momentum transfer events. The scatter in  $\theta$  and  $\phi$  was essentially due to neutron evaporation from the fragments as well as events corresponding to the incomplete fusion-fission events, called transfer fission (TF). The mass distributions have been obtained by using a gate, as shown by a black square in the figure, to ensure full momentum transfer events. Figure 2 shows a representative plot of the measured mass total kinetic-energy correlation of the fission fragments in the reactions  $^{20}\text{Ne} + ^{205}\text{Tl}$  and  $^{16}\text{O} + ^{209}\text{Bi}$  at an excitation energy  $\approx 83$  MeV. It can be observed that the mass-energy distributions show typical LDM behavior.

The mass distributions for both reactions are found to be symmetric in nature at all measured energies, as shown in

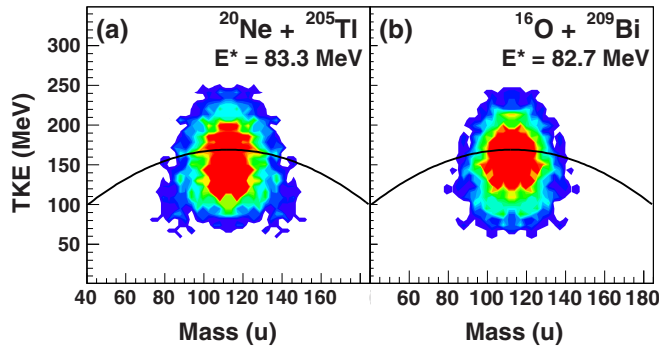


FIG. 2. The representative measured mass total kinetic-energy correlation plot of the fission fragments in the reactions  $^{20}\text{Ne} + ^{205}\text{Tl}$  and  $^{16}\text{O} + ^{209}\text{Bi}$  at excitation energy  $\approx 83$  MeV. The black curve represents the expected parabolic dependence.

Fig. 3. The distributions could be fit by a single Gaussian curve, as indicated by the solid (red) line, with the peak near half of the total mass of the target and projectile. It is known that, when quasifission or fast-fission is present, the mass distribution tends to be asymmetric (with higher yields around the target and projectile masses), and this causes the width of the distributions to be larger compared with the compound nuclear fission where mass distributions are symmetric. A sudden increase in the width of the mass distribution is a signature of the onset of quasifission [18,20].

The variation of the standard deviations  $\sigma_m(u)$  of the fitted experimental mass distributions are shown as a function of excitation energy in Fig. 4. For both the  $^{20}\text{Ne} + ^{205}\text{Tl}$  and  $^{16}\text{O} + ^{209}\text{Bi}$  reactions,  $\sigma_m(u)$  increases smoothly with excitation energy and there is no large-scale abnormal deviation in  $\sigma_m(u)$  at higher excitation energies. It is to be mentioned here that, for the similar reactions  $^{19}\text{F} + ^{181}\text{Ta}$  and  $^{16}\text{O} + ^{184}\text{W}$ , a significant amount of quasifission and fast-fission were predicted by Nasirov *et al.* [13] from theory at a similar energy range as studied in this work. On a qualitative level, this should have shown up as an unusual increase in the width of the mass distributions for the measured systems in this work, but this was not noticed at all.

In the case of compound nuclear fission, the variance  $\sigma_m^2(u)$  of the fission-fragment mass distribution is a linear function of the nuclear temperature. The standard deviation of the mass distribution, according to statistical theory [21], is given by

$$\sigma_m = \sqrt{T/k}, \quad (1)$$

where the scission-point temperature is  $T$ , and the stiffness parameter for mass asymmetry is  $k$ . The standard deviation of the mass distributions was calculated using the saddle-point temperature rather than the scission-point temperature since the two temperatures are comparable [22] for the two systems studied in this work. The temperature of the fissioning nucleus at the saddle point can be determined as

$$T = \{[E^* - B_f(l) - E_{\text{pre}} - E_{\text{rot}}]/a\}^{1/2}, \quad (2)$$

in which  $E^*$  is the excitation energy of the compound nucleus,  $B_f(l)$  is the angular-momentum-dependent height of the fission barrier,  $E_{\text{rot}}$  is the rotational energy of compound nucleus

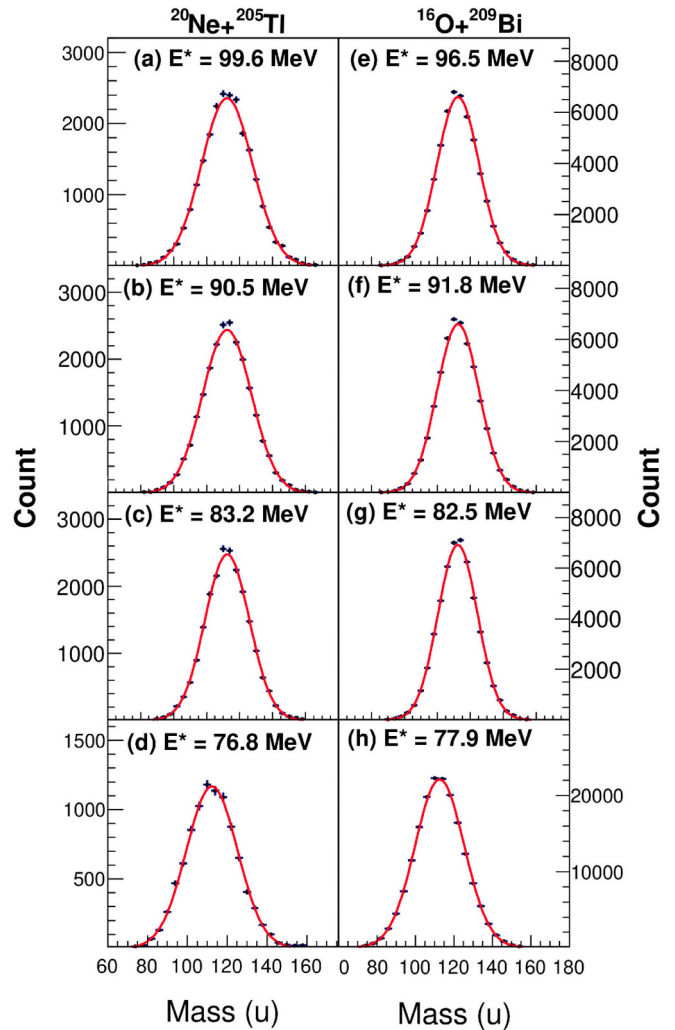


FIG. 3. The measured mass distributions of fission fragments in the reactions  $^{20}\text{Ne} + ^{205}\text{Tl}$  and  $^{16}\text{O} + ^{209}\text{Bi}$  at different excitation energies. The distributions were well fit with a single Gaussian, as shown by the solid lines (red).

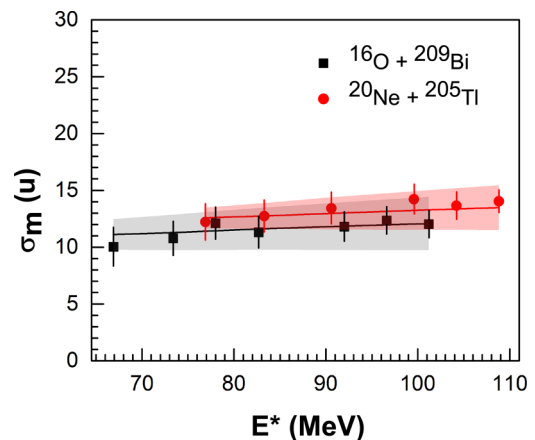


FIG. 4. Variation of the standard deviation  $\sigma_m(u)$  of the fitted symmetric mass distribution with excitation energy. The calculated widths are shown by solid lines, the shaded regions indicate uncertainties in the calculation (see text).

TABLE I. The reaction parameters for  $^{20}\text{Ne} + ^{205}\text{Tl}$  and  $^{16}\text{O} + ^{209}\text{Bi}$  are presented;  $\langle \ell \rangle$ ,  $\langle \ell^2 \rangle$ , and  $\ell_{cr}$  are the values of the average angular momentum, square of the average angular momentum [25], and the critical angular momentum [26–28].

Reaction	$E_{\text{lab}}$ (MeV)	$E^*$ (MeV)	$\langle \ell \rangle$ ( $\hbar$ )	$\langle \ell^2 \rangle$ ( $\hbar^2$ )	$\ell_{cr}$ ( $\hbar$ )
$^{20}\text{Ne} + ^{205}\text{Tl}$	138	70.5	39.5	1560.25	59.4
	145	76.9	43.2	1863.6	64.7
	152	83.3	49.4	2165.0	69.4
	160	90.6	50.1	2505.0	73.9
	170	99.6	54.1	2922.5	78.4
	175	104.2	55.9	3125.9	80.5
	180	108.8	57.7	3332.8	82.6
	$^{16}\text{O} + ^{209}\text{Bi}$	123	66.9	37.6	1415.3
126		69.7	39.0	1521.0	58.1
130		73.4	40.6	1660.6	60.5
135		78.0	42.8	1835.3	63.3
140		82.7	44.8	2005.2	65.4
150		92.0	48.4	2344.5	69.5
155		96.6	50.1	2510.0	71.4
160		101.2	51.8	2679.1	73.3

(CN) at the saddle point, calculated using the finite-range rotating liquid-drop model [23],  $E_{\text{pre}}$  is the energy carried by prefission neutrons (typically 3 to 4) estimated using the empirical systematic [24], and  $a = A/8.5$  [9] denotes the level-density parameter.

The width of the mass distribution also depends on the mean-square average value of angular momentum,  $\langle \ell^2 \rangle$  as :

$$\sigma_m(\mathbf{u}) = \sqrt{(T/k + \beta \langle \ell^2 \rangle)}, \quad (3)$$

where  $T$  is the saddle-point temperature and the constant value of  $\beta \approx 0.05$  was used [22]. The CCFULL code was used to determine  $\langle \ell^2 \rangle$  of the CN [25]. The calculated values are presented in Table I. A good fit to the data, as seen in Fig. 4, could be achieved by using the inverse stiffness parameter  $1/k = (98.1 \pm 15.1) \text{ u}^2/\text{MeV}$ . The value of  $k$  used here was found to be consistent with the comprehensive compilation of the earlier data [22]. The gray and red shaded areas in Fig. 4 show the uncertainty in the computation of  $\sigma_m$  caused by the uncertainty in the value of the inverse stiffness parameter  $1/k$ . Within the boundaries of uncertainty, mass variances of both systems seem to have followed a similar path. In the case of pure statistical fission (with no shell effect), the width  $\sigma_m$  increases only slowly with  $T$  (or  $E^*$ ), as can be seen from Eq. (3). On the other hand, the value of  $\sigma_m$  would abruptly change if there is any change in the reaction mechanism (e.g., onset of quasifission). Since neither system showed any such anomaly in the variation of the width of the mass distribution, the present measurement suggests that there is no evidence of noncompound nuclear reactions (QF or fast-fission). While comparing the  $^{16}\text{O} + ^{209}\text{Bi}$  reaction to the  $^{20}\text{Ne} + ^{205}\text{Tl}$  reaction at the same excitation energy, the slight increase in the width of the mass distribution may be attributed to the heavier  $^{20}\text{Ne}$  beam that brings more angular momentum.

## IV. DISCUSSION

### A. Role of angular momentum: HICOL calculation

The present study was carried out with beams of incident energies almost 30% above the Coulomb barrier and higher. The angular momentum induced at such energies is quite large, nearing the critical angular momentum corresponding to the disappearance of the pocket of the nucleus-nucleus potential. The capture of the projectile by the target nucleus is related to the depth of this pocket. Hence, an examination of the role of angular momentum on the dynamics at play for such high excitation energies is also of interest.

Noncompound processes are highly sensitive to the angular momentum of the composite formed, e.g., fast-fission originates at high angular momentum when the fission barrier of the hot and rotating compound nucleus disappears. Quasifission is also a process which is very sensitive to angular momentum [29,30] as the barriers governing the fusion and quasifission dynamics across the potential-energy surface are sensitive to angular momentum. Hence, the evolution of the reacting system is expected to be influenced by the angular momentum.

An analysis was carried out using the HICOL code [31,32] for both reactions to trace the time evolution of the composite system at a representative excitation energy  $\approx 70$  MeV. The HICOL code does not contain any free parameters and has earlier been shown to consistently describe the dynamical evolution of various composite systems formed in nucleus-nucleus collisions [33]. The internuclear distance between the target and the projectile has been calculated with time corresponding to different angular momenta as shown in Fig. 5. The angular momentum has been sampled based on the partial cross section calculated using the CCFULL code, as discussed in the preceding section. In Fig. 5, the shaded regions correspond to a composite with an internuclear size corresponding to  $R_0 A^{1/3}$ , which represents the size of a spherical compound nucleus. Thus, it may be inferred that the composite attaining a size comparable to the compound nucleus may proceed towards equilibration in all degrees of freedom. However, a composite with a size larger than compound nucleus dimensions indicates the presence of noncompound processes. From the calculation, it may be inferred that for trajectories with high angular momentum (e.g.,  $l = 63$  for  $^{16}\text{O} + ^{209}\text{Bi}$  and  $l = 58, 66$  for  $^{20}\text{Ne} + ^{205}\text{Tl}$ , as shown in Fig. 5) there may exist some noncompound process for both reactions. The indication of the presence of noncompound fission in either of the two reactions is further confirmed by our following calculation.

### B. Calculation of potential energy surface: The driving potential

Using the components binding energies and their interfacial potential energies, the potential-energy surface (PES)—the path at which the system evolves—is calculated. The landscape of PES plays the main role in the estimation of the complete fusion probability in competition with quasifission. The mass, charge, deformation, and microscopic structure of the interacting nuclei are the key determinants of the PES characteristics [3,30]. These, in turn, affect the likelihood of

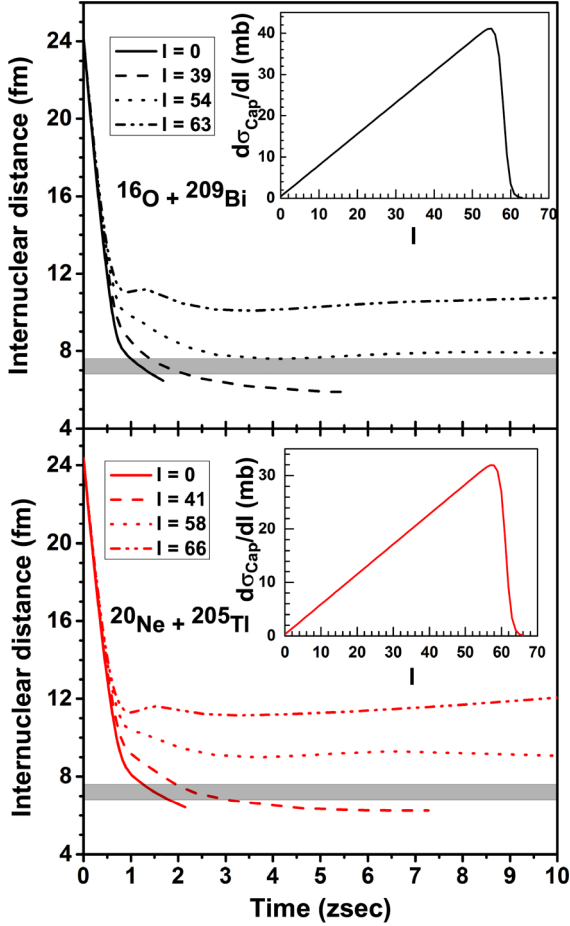


FIG. 5. Time evolution of the composite systems at different angular momentum using HICOL code. The insets show the angular-momentum distributions for capture calculated using CCFULL. The shaded regions correspond to a composite with an internuclear size corresponding to a spherical compound nucleus produced in complete fusion (see text).

capture. The capture probability and subsequent development of the dinuclear system (DNS) are influenced by the beam energy, rotational momentum, and intensity of the dissipative forces. The sticking time of the dinuclear system after capture is another significant component that affects how the response turns out. If the DNS does not remain intact for a long enough period of time for all degrees of freedom to be balanced, nonequibrated products like quasifission will occur, in which the DNS breaks into fission-like components.

The inherent fusion barrier  $B_{\text{fus}}^*$  for the conversion of the DNS into the CN is connected to the impediment to full fusion in the scope of the model utilized in this study. By getting through the quasifission barrier  $B_{\text{qf}}$ , the DNS eventually breaks apart into two pieces. The quasifission barrier  $B_{\text{qf}}$  is determined by the depth of the potential well of the nucleus-nucleus interaction. These variables ( $B_{\text{fus}}^*$  and  $B_{\text{qf}}$ ) are defined by the landscape of the PES, which are computed using the following formula for the given values of angular momentum  $l$  and orientation angles  $\{\alpha_i\}$  of the colliding nuclei

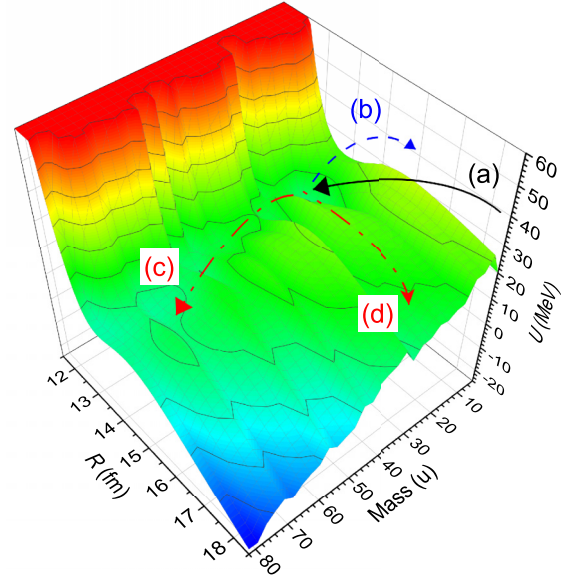


FIG. 6. The potential-energy surface calculated for  $^{225}\text{Pa}$  is shown as a function of the distance ( $R$ ) between the interacting nuclei and charge numbers ( $Z$ ) of the fragments for the angular momentum  $l = 40$ . Arrow (a) shows the capture path in the entrance channel; arrow (b) represents the fusion path; arrows (c) and (d) show the directions of decay of DNS into QF channels. The potential-energy surface is calculated for the orientation angles  $\alpha_1 = 45^\circ$  and  $\alpha_2 = 30^\circ$ .

[30,34]:

$$U(Z, A, \ell, \{\alpha_i\}, R) = \Delta Q_{\text{gg}}^{(Z, A)} + V(Z, A, l, \{\alpha_i\}, R) - V_{\text{rot}}^{\text{CN}}(l), \quad (4)$$

where  $\Delta Q_{\text{gg}}^{(Z, A)} = B_P + B_T - (B_Z + B_{Z_{\text{tot}}-Z})$  is the reaction energy balance;  $B_P + B_T$  and  $B_Z + B_{Z_{\text{tot}}-Z}$  are sums of the binding energies of the colliding projectile-target nuclei and DNS fragments with charge ( $Z$ ) and mass ( $A$ ) numbers, respectively, which are obtained from the nuclear mass tables in Refs. [35,36].  $Z_{\text{tot}} = Z_P + Z_T$  and  $A_{\text{tot}} = A_P + A_T$  are total charge and mass number of the system. The corresponding mass numbers  $A$  are found by the minimization of the total energy of the DNS as a function of  $A$ . The nucleus-nucleus potential  $V(Z_1, A_1, Z_2, A_2, \ell, \{\alpha_i\}, R)$  consists of three parts:

$$V(Z, A, l, \{\alpha_i\}, R) = V_{\text{Coul}}(Z, A, l, \{\alpha_i\}, R) + V_{\text{nucl}}(Z, A, l, \{\alpha_i\}, R) + V_{\text{rot}}(Z, A, l, \{\alpha_i\}, R), \quad (5)$$

where  $V_{\text{Coul}}$ ,  $V_{\text{nucl}}$ , and  $V_{\text{rot}}$  are the nuclear, Coulomb, and rotational potentials, respectively. The procedures for calculating these three components of the nucleus-nucleus potential as a function of the orientation angles of the colliding nuclei are discussed explicitly in Refs. [11,34].

In Fig. 6, the PES calculated for  $^{225}\text{Pa}$  is shown as an example, for  $l = 40$ . The capture, fusion, and one of the probable quasifission paths are shown in the figure. Arrows (a) and (b) illustrate the direction of full fusion via multinucleon transfer from the light nucleus to the heavy one, respectively,

whereas arrows (c) and (d) represent the paths of DNS decay into mass asymmetric quasifission channel. From such a PES calculated for a given  $l$ , we calculate the driving potential  $U_{dr}$  by connecting all the minima in the PES, for all values of  $A$ .

### C. Estimation of quasifission yield

We use the same theoretical model [13] that was used to predict the presence of quasifission in the similar reactions  $^{19}\text{F} + ^{181}\text{Ta}$  and  $^{16}\text{O} + ^{184}\text{W}$  [14]. The transport master equations have been used to calculate the mass and charge distribution [30] for the  $^{20}\text{Ne} + ^{205}\text{Tl}$  and  $^{16}\text{O} + ^{209}\text{Bi}$  reactions. The characteristics of the mass distribution of the reaction products are defined by the PES of the nuclear system, the shell structure of protons and neutrons in nuclei, and the DNS excitation energy. The lifetime of the DNS is longer in QF compared with deep-inelastic collisions and the nucleon exchange takes place between fragments of the DNS before its decay and during its transformation into a compound nucleus. The charge and mass numbers of a DNS fragment are changed from those of the projectile and target nuclei.

Both in the QF and fusion-fission processes, the intense mass transfer takes place and depending upon the entrance channel, the mass asymmetry degree of freedom may be fully or partially equilibrated. As a result, we have an ensemble  $Z$  of the DNS, which contributes to the competition between complete fusion and quasifission with  $Y_Z$  probabilities. The charge and mass configuration of the DNS is continuously changed due to nucleon transfer between its fragments up to complete fusion or its breakup. The time dependence of the charge distribution is calculated by the master transport equation with the transition coefficients  $\Delta_Z^{(\pm)}(A_Z, E_Z^*)$  which are calculated by the microscopic method allowing us to include the single-particle structure of the DNS fragments and their excitation energy [30]. The evolution of the charge distribution  $D_Z$  between the DNS fragments at its excitation energy  $E_Z^*$  is estimated by the solution of the transport master equation [30,34]:

$$\begin{aligned} \frac{\partial}{\partial t} D_Z(E_Z^*, A_Z, t) &= \Delta_{Z+1}^{(-)}(A_{Z+1}, E_{Z+1}^*) D_{Z+1}(E_{Z+1}^*, t) \\ &+ \Delta_{Z-1}^{(+)}(A_{Z-1}, E_{Z-1}^*) D_{Z-1}(A_{Z-1}, E_{Z-1}^*, t) \\ &- [\Delta_Z^{(-)}(A_Z, E_Z^*) + \Delta_Z^{(+)}(A_Z, E_Z^*) \\ &+ \Lambda_{\text{qf}}(Z, A_Z, E_Z^*)] D_Z(A_Z, E_Z^*, t), \end{aligned} \quad (6)$$

where  $Z = 2, 3, \dots, Z_{\text{tot}} - 2$  and the transition coefficients  $\Delta_Z^{(\pm)}(A_Z, E_Z^*)$  determine the probability of nucleon transfer between the DNS nuclei characterized with the charge (mass) numbers  $Z(A)$  and  $Z_{\text{tot}} - Z(A_{\text{tot}} - A)$ ;  $E_Z^*$  is its excitation energy which is determined by the initial collision energy  $E_{c.m.}$ , the minimum value of the potential well  $V_{\text{min}}^{(Z)}$  in the nucleus-nucleus interaction and the energy balance of the nucleon transfer  $\Delta Q_{gg}^{(Z,A)}$ :

$$E_Z^* = E_{c.m.} - V_{\text{min}}^{(Z,A)} + \Delta Q_{gg}^{(Z,A)}. \quad (7)$$

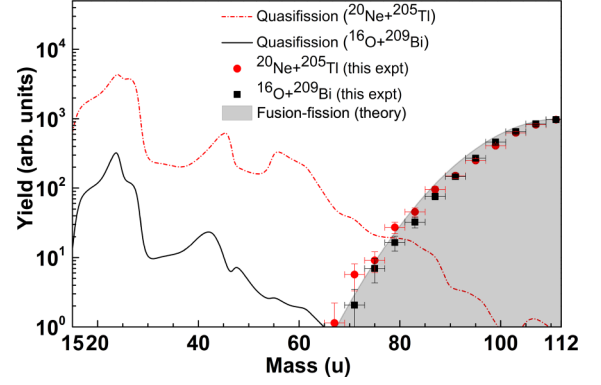


FIG. 7. Calculated mass distributions up to the symmetric mass ( $A_{\text{CN}}/2 \approx 112$ ) at the excitation energy  $\approx 83$  MeV. The normalized fusion-fission yield (produced in both reactions) is shown by the shaded area and have been compared with the experimental data. The quasifission yields for  $^{20}\text{Ne} + ^{205}\text{Tl}$  and  $^{16}\text{O} + ^{209}\text{Bi}$  reactions are shown by dashed (blue) and solid (red) lines, respectively.

The yield of the quasifission product with the charge ( $Z$ ) and mass ( $A = A_Z$ ) numbers is calculated by the formula

$$\begin{aligned} Y_Z(E_Z^*, A, t) &= \sum_{l=0}^{l=l_d} \Lambda_{\text{qf}}(Z, A, l) (B_{\text{qf}}^{\text{qf}}(Z, A, T_Z(A, l))) \\ &\times \sum_{k=0}^{k_{\text{max}}} D_Z(A, E_Z^*, l, t_0 + k \Delta t). \end{aligned} \quad (8)$$

$\Lambda_{\text{qf}}(Z, A_Z)$  is the Kramers rate for the decay probability of the DNS into two fragments with charge numbers  $Z$  and  $Z_{\text{tot}} - Z$  [37] and it is proportional to  $\exp(-B_{\text{qf}}(Z, A)/T_Z)$  where  $B_{\text{qf}}(Z, A)$  is the QF (pre-scission) barrier against decay and  $T_Z$  is the effective temperature of the system:  $T_Z = 3.46(12E_Z^*/A_{\text{tot}})^{1/2}$ . Details of the calculation of the transition coefficients of multinucleon transfer are reported in Refs. [30,34]. The quasifission barrier  $B_Z^{\text{qf}}$  and excitation energy  $E_Z^*$  of the DNS are determined by its PES landscape which depends on the angular momentum  $l$ . Therefore, the yield  $Y_Z$  of the quasifission products depends on the angular momentum, the shell structure of the fragments, and peculiarities of the PES calculated by Eq. (4) in Sec. IV B. The contribution of the QF products to the yield of the  $^{20}\text{Ne} + ^{205}\text{Tl}$  and  $^{16}\text{O} + ^{209}\text{Bi}$  reactions products at different energies have been estimated by the numerical solution of Eq. (4) with the initial conditions  $Y_Z(Z_P = 8, 10) = 1$  and  $Y_Z(Z_T = 205, 209) = 1$ . We use  $\Delta t = 10^{-22}$  s for these calculations.

In Fig. 7 we show the representative plot of the calculated yields of the events originating from fusion-fission and QF at the excitation energy of  $\approx 83$  MeV for the measured reactions. To compare the experimental mass distribution with the theoretical prediction, a set of normalization steps were applied. In the first step, the experimental mass distribution was normalized with a factor such that the yield of the mass of half the compound nuclear mass ( $A_{\text{CN}}/2$ ) was set to 1000 (arbitrary units). In the second step, the same procedure was applied to the theoretical mass yields, with a normalization factor

determined such that the yield at  $(A_{CN}/2)$  was set to 1000. The same factor obtained in step 2, was applied to the theoretical quasifission yield distribution. This ensures that the data from the experiment and the theoretical prediction are compared on the same scale. The distributions of the calculated and measured fusion-fission yields match well for both reactions. Calculated QF yields are observed in the asymmetric mass region with the maximum yield near the projectile mass where the data could not be collected (discussed in the following section). For the  $^{20}\text{Ne} + ^{205}\text{Tl}$  reaction QF yield extends even up to the symmetric mass, however, the contribution of QF to the overlap region with the fusion-fission mass distributions is less than 5%. The calculation indicates QF in  $^{16}\text{O} + ^{209}\text{Bi}$  reaction originates in the asymmetric region only.

#### D. Perspective on further measurement and theoretical calculation

We are at the interesting juncture to note that while experimentally observed smooth variation of the width of the mass distribution with excitation energy, as shown in Fig. 4 indicates an absence of quasifission, theoretical calculations performed in the framework of the dinuclear system [13] predict the presence of quasifission for both the reactions. It is significant to observe from Fig. 7 that the calculated quasifission events are in the asymmetric mass region; in particular, the maximum yield is near the projectile mass region.

In the standard method of the measurement of the mass distributions, emphasis is given to getting rid of the projectile-like events. Thus, in the present measurement, as done in any other measurement of fission-fragment mass distributions, efforts were expended to not detect projectile-like events by using gas detectors operating at lower pressure. Since the measured width of the mass distributions in the experiment is calculated only from the detected symmetric events, it may not reflect the prediction of theoretical model calculations that consider all (projectile-, target-like, and symmetric fragments) events. However, the DNS model works well in the symmetric mass range covered in the measurement.

The detection of events in the projectile- and target-like masses, particularly for light projectiles, is challenging in any measurement due to the large elastic flux. The theoretical calculations carried out in the framework of the DNS model warrant investigation of the fusion-fission process for similar reactions through the measurement of projectile-like events

(though challenging) or other observables like measurement of evaporation residue (ER) cross section, where the presence of the quasifission process would be indicated through a suppressed ER value compared with theory [13]. However, new calculations in the framework other than the dinuclear system model as used here may also shed more light about the presence of very asymmetric fission fragments in the reactions studied in this work.

#### V. CONCLUSIONS

To sum up, fission-fragment mass distributions in the  $^{20}\text{Ne} + ^{205}\text{Tl}$  and  $^{16}\text{O} + ^{209}\text{Bi}$  reactions have been measured over excitation energy range of  $\approx 70\text{--}110$  MeV. The fragment mass widths for both the systems studied, irrespective of the entrance channels, showed identical trends and the variations of the widths of the mass distribution were found within the limit of the statistical model calculation. Thus the measurement indicated the absence of quasifission contribution in the symmetric mass distribution range for both reactions. The theoretical calculation performed in the framework of the dinuclear system model, however, showed the contribution of quasifission in the mass distribution mainly near the projectile and target mass. Nevertheless, for the  $^{20}\text{Ne} + ^{205}\text{Tl}$  reaction, QF yield extends even up to the symmetric mass, although the contribution of QF to the overlap region with the fusion-fission mass distributions is less than 5%.

The present investigation calls for the detection of quasifission events, if any, through the measurement of projectile-like fragments, or other probes like measurement of ER cross-section to test the reliability of the theoretical models to understand the dynamics of quasifission and fusion-fission reaction mechanism. New theoretical calculations may also be helpful to investigate the presence of very asymmetric fission fragments in reactions studied in this work.

#### ACKNOWLEDGMENTS

The authors take this opportunity to thank all accelerator staff of VECC Kolkata for providing a good-quality beam. J. K. Meena, A. K. Saha, J. K. Sahoo, S. Dalal, and R. M. Saha are thanked for their help in the experiment. Illuminating discussions with Dr. Jhilam Sadhukhan are gratefully acknowledged. We thank Dr. S. Bhattacharya for critically reading the paper.

- 
- [1] E. Vardaci, M. G. Itkis, I. M. Itkis, G. Knyazheva, and E. M. Kozulin, *J. Phys. G* **46**, 103002 (2019).
  - [2] D. J. Hinde, M. Dasgupta, and E. C. Simpson, *Prog. Part. Nucl. Phys.* **118**, 103856 (2021).
  - [3] G. Fazio, G. Giardina, G. Mandaglio, R. Ruggeri, A. I. Muminov, A. K. Nasirov, Yu. Ts. Oganessian, A. G. Popeko, R. N. Sagaidak, A. V. Yeremin, S. Hofmann, F. Hanappe, and C. Stodel, *Phys. Rev. C* **72**, 064614 (2005).
  - [4] A. K. Nasirov, G. Mandaglio, G. Giardina, A. Sobiczewski, and A. I. Muminov, *Phys. Rev. C* **84**, 044612 (2011).
  - [5] G. G. Adamian, N. V. Antonenko, and W. Scheid, *Eur. Phys. J. A* **41**, 235 (2009).
  - [6] V. I. Zagrebaev and W. Greiner, *Nucl. Phys. A* **944**, 257 (2015).
  - [7] S. Bjørnholm and W. J. Swiatecki, *Nucl. Phys. A* **391**, 471 (1982).
  - [8] J. Töke, R. Bock, G. X. Dai, A. Gobbi, S. Gralla, K. D. Hildenbrand, J. Kuzminski, W. F. J. Müller, A. Olmi, H. Stelzer, B. B. Back, and S. Bjørnholm, *Nucl. Phys. A* **440**, 327 (1985).
  - [9] B. B. Back, R. R. Betts, J. E. Gindler, B. D. Wilkins, S. Saini, M. B. Tsang, C. K. Gelbke, W. G. Lynch, M. A. McMahan, and P. A. Baisden, *Phys. Rev. C* **32**, 195 (1985).

- [10] V. S. Ramamurthy and S. S. Kapoor, *Phys. Rev. Lett.* **54**, 178 (1985).
- [11] G. Fazio, G. Giardina, A. Lamberto, R. Ruggeri, C. Saccá, R. Palamara, A. I. Muminov, A. K. Nasirov, U. T. Yakhshiev, F. Hanappe, T. Materna, and L. Stuttgé, *J. Phys. Soc. Jpn.* **72**, 2509 (2003).
- [12] M. G. Itkis, E. Vardaci, I. M. Itkis, G. N. Knyazheva, and E. M. Kozulin, *Nucl. Phys. A* **944**, 204 (2015).
- [13] A. Nasirov, G. Mandaglio, M. Manganaro, A. Muminov, G. Fazio, and G. Giardina, *Phys. Lett. B* **686**, 72 (2010).
- [14] A. Chaudhuri, A. Sen, T. K. Ghosh, K. Banerjee, J. Sadhukhan, S. Bhattacharya, P. Roy, T. Roy, C. Bhattacharya, M. A. Asgar, A. Dey, S. Kundu, S. Manna, J. K. Meena, G. Mukherjee, R. Pandey, T. K. Rana, V. Srivastava, R. Dubey, G. Kaur *et al.*, *Phys. Rev. C* **94**, 024617 (2016).
- [15] Rajni, R. Kumar, and M. K. Sharma, *Phys. Rev. C* **90**, 044604 (2014).
- [16] V. E. Viola, K. Kwiatkowski, and M. Walker, *Phys. Rev. C* **31**, 1550 (1985).
- [17] T. K. Ghosh *et al.*, *Nucl. Instrum. Methods Phys. Res., Sect. A* **540**, 285 (2005).
- [18] T. K. Ghosh *et al.*, *Phys. Lett. B* **627**, 26 (2005).
- [19] A. Choudhury, Dynamics of fusion fission reactions near Coulomb barrier, Ph.D. thesis, The Homi Bhabha National Institute, 2018.
- [20] R. G. Thomas, D. J. Hinde, D. Duniec, F. Zenke, M. Dasgupta, M. L. Brown, M. Evers, L. R. Gasques, M. D. Rodriguez, and A. Diaz-Torres, *Phys. Rev. C* **77**, 034610 (2008).
- [21] B. B. Back, P. B. Fernandez, B. G. Glagola, D. Henderson, S. Kaufman, J. G. Keller, S. J. Sanders, F. Videbæk, T. F. Wang, and B. D. Wilkins, *Phys. Rev. C* **53**, 1734 (1996).
- [22] G. N. Knyazheva, E. M. Kozulin, R. N. Sagaidak, A. Y. Chizhov, M. G. Itkis, N. A. Kondratiev, V. M. Voskressensky, A. M. Stefanini, B. R. Behera, L. Corradi, E. Fioretto, A. Gadea, A. Latina, S. Szilner, M. Trotta, S. Beghini, G. Montagnoli, F. Scarlassara, F. Haas, N. Rowley *et al.*, *Phys. Rev. C* **75**, 064602 (2007).
- [23] A. J. Sierk *et al.*, *Phys. Rev. C* **33**, 2039 (1986).
- [24] M. G. Itkis and A. Y. Rusanov, *Phys. Part. Nucl.* **29**, 160 (1998).
- [25] K. Hagino, N. Rowley, and A. T. Kruppa, *Comput. Phys. Commun.* **123**, 143 (1999).
- [26] R. J. Charity, L. G. Sobotka, J. Cibor, K. Hagel, M. Murray, J. B. Natowitz, R. Wada, Y. El Masri, D. Fabris, G. Nebbia, G. Viesti, M. Cinausero, E. Fioretto, G. Prete, A. Wagner, and H. Xu, *Phys. Rev. C* **63**, 024611 (2001).
- [27] R. J. Charity, *Phys. Rev. C* **82**, 014610 (2010).
- [28] D. Mancusi, R. J. Charity, and J. Cugnon, *Phys. Rev. C* **82**, 044610 (2010).
- [29] S. Mohsina and J. Sadhukhan, *Phys. Rev. C* **101**, 044607 (2020).
- [30] A. Nasirov, K. Kim, G. Mandaglio, G. Giardina, A. Muminov, and Y. Kim, *Eur. Phys. J. A* **49**, 147 (2013).
- [31] H. Feldmeier, *Rep. Prog. Phys.* **50**, 915 (1987).
- [32] K. Siwek-Wilczyńska, J. Wilczyński, R. H. Siemssen, and H. W. Wilschut, *Phys. Rev. C* **51**, 2054 (1995).
- [33] C. Schmitt, K. Mazurek, and P. N. Nadtochy, *Phys. Rev. C* **97**, 014616 (2018).
- [34] A. Nasirov, A. Fukushima, Y. Toyoshima, Y. Aritomo, A. Muminov, S. Kalandarov, and R. Utamuratov, *Nucl. Phys. A* **759**, 342 (2005).
- [35] G. Audi and A. H. Wapstra, *Nucl. Phys. A* **595**, 409 (1995).
- [36] P. Möller, J. R. Nix, W. D. Meyers, and W. J. Swiatecki, *At. Data Nucl. Data Tables* **59**, 185 (1995).
- [37] G. G. Adamian, N. V. Antonenko, and W. Scheid, *Phys. Rev. C* **68**, 034601 (2003).